

## HECS-SZ: THE HECTOSPEC SURVEY OF SUNYAEV-ZELDOVICH SELECTED CLUSTERS

KENNETH J. RINES<sup>1</sup>, MARGARET J. GELLER<sup>2</sup>, ANTONALDO DIAFERIO<sup>3,4</sup>, AND HO SEONG HWANG<sup>5</sup>

*Draft version July 31, 2018*

### ABSTRACT

We estimate cluster masses and velocity dispersions for 123 clusters from optical spectroscopy to compare the Sunyaev-Zeldovich (SZ) mass proxy and dynamical masses. Our new survey, HeCS-SZ (Hectospec Cluster Survey of SZ-selected clusters), includes 7,721 new or remeasured redshifts from MMT/Hectospec observations of 24 SZ-selected clusters at redshifts  $z=0.05-0.20$  and not in previous surveys. We supplement the Hectospec data with spectra from the Sloan Digital Sky Survey (SDSS) and cluster data from the Cluster Infall Regions in SDSS (CIRS) project and the Hectospec Cluster Survey (HeCS), our Hectospec survey of clusters selected by X-ray flux. We measure the scaling relation between velocity dispersion and SZ mass estimates from the integrated Compton parameter for an SZ complete sample of 83 clusters. The observed relation agrees very well with a simple virial scaling from mass (based on SZ) to velocity dispersion. The SZ mass estimates (calibrated with hydrostatic X-ray mass estimates) are not significantly biased. Further, the velocity dispersion of cluster galaxies is consistent with the expected velocity dispersion of dark matter particles, indicating that galaxies are good dynamical tracers (i.e., velocity bias is small). Significant mass bias in SZ mass estimates could relieve tension between cosmological results from *Planck* SZ cluster counts and *Planck* CMB data. However, the excellent agreement between our measured velocity dispersions and those predicted from a virial scaling relation suggests that any SZ mass bias is too small to reconcile SZ and CMB results. In principle, SZ mass bias and velocity bias of galaxies could conspire to yield good agreement, but the required velocity bias is  $\sigma_{galaxy} \approx 0.77\sigma_{DM}$ , outside the range of plausible models of velocity bias in the literature.

*Subject headings:* galaxies: clusters: individual — galaxies: kinematics and dynamics — cosmology: observations

### 1. INTRODUCTION

As the universe evolves, the comoving number density of clusters of fixed mass increases. The evolution of cluster abundances depends strongly on the amount of dark matter and dark energy in the universe. Thus, many groups have used different cluster mass proxies to determine the mass function and constrain cosmological parameters (e.g., Rines et al. 2007, 2008; Vikhlinin et al. 2009b; Henry et al. 2009; Mantz et al. 2010b; Rozo et al. 2010, and references therein). Recently, others have used the Sunyaev-Zeldovich (SZ) effect (Sunyaev & Zeldovich 1972) to identify large samples of clusters to constrain cosmological parameters (Benson et al. 2013; Hasselfield et al. 2013; Planck Collaboration et al. 2014b,a).

Data from the *Planck* satellite show that cosmological parameters determined from anisotropies in the cosmic microwave background disagree with those derived from cluster abundance measurements from the *Planck* SZ cluster survey (Planck Collaboration et al. 2014a, 2015a). Fewer clusters are observed than predicted by the cosmology that best fits the *Planck* CMB data. Inter-

estingly, estimates of the amplitude of structure from cosmic shear yield a similar tension with *Planck* CMB data (MacCrann et al. 2015). If SZ masses (calibrated from X-ray observations) systematically underestimate true masses by about 45%, the cosmological parameters derived from SZ cluster counts shift into agreement with the CMB results (Planck Collaboration et al. 2014a). An alternate analysis using weak lensing data for mass calibration finds no significant tension (von der Linden et al. 2014; Mantz et al. 2015), suggesting that the tension could arise from biases in the calibration of SZ masses.

Here, we compare SZ mass estimates to dynamical mass estimates based on the redshifts of cluster members. Dynamical mass estimates have a long history beginning with Zwicky (1933, 1937). In numerical simulations, either the virial theorem or the caustic technique can provide cluster mass estimates with little bias but with some intrinsic scatter due to projection effects (Diaferio 1999; Evrard et al. 2008; Serra et al. 2011; Mamon et al. 2013; Gifford & Miller 2013; Old et al. 2014). Hydrodynamical simulations show that the velocity distribution of galaxies is very similar to that of dark matter particles (Faltenbacher & Diemand 2006; Lau et al. 2010), with the possible exception of the brightest few galaxies (Lau et al. 2010; Wu et al. 2013). Thus, virial masses, caustic masses, or dynamical mass proxies such as velocity dispersion are a powerful test of SZ mass estimates.

Rines et al. (2010) made the first comparison of SZ signals to mass estimates from galaxy dynamics, but the sample was limited to 15 clusters. A later study by Sifón et al. (2013) obtained optical spectroscopy for 16 SZ-selected clusters selected from observations with

kenneth.rines@wwu.edu

<sup>1</sup> Department of Physics & Astronomy, Western Washington University, Bellingham, WA 98225; kenneth.rines@wwu.edu

<sup>2</sup> Smithsonian Astrophysical Observatory, 60 Garden St, Cambridge, MA 02138

<sup>3</sup> Università di Torino, Dipartimento di Fisica, Torino, Italy

<sup>4</sup> Istituto Nazionale di Fisica Nucleare (INFN), Sezione di Torino, Torino, Italy

<sup>5</sup> School of Physics, Korea Institute for Advanced Study, 85 Hoegiro, Dongdaemun-Gu, 130-722 Seoul, Korea

the Atacama Cosmology Telescope (ACT); they found that the scaling relation between SZ signal and mass (actually measured from velocity dispersions) is consistent with relations determined with other mass calibrators (X-ray, lensing). Ruel et al. (2014) measured velocity dispersions for SZ-selected clusters identified in observations with the South Pole Telescope (SPT); they conclude that SZ signal correlates well with velocity dispersion. The SPT results (Bocquet et al. 2015) are consistent with positive velocity bias (that is, the velocity dispersion of the galaxies is larger than the velocity dispersion of the dark matter particles). The clusters in the ACT and SPT samples span a wide range of redshifts ( $0.2 < z < 1.3$ ). It is possible that the scaling between velocity dispersion and virial mass evolves significantly over that period. Further, the spectroscopy for these clusters is often incomplete at large radii or contains relatively few cluster members. In principle, the measured velocity dispersions could be biased (e.g., Biviano et al. 2006; Wu et al. 2013).

To provide a much broader foundation for comparison of dynamical and SZ mass proxies, we compare SZ mass estimates of 123 clusters from the *Planck* SZ catalog with velocity dispersions from wide-field optical spectroscopy. Several clusters have redshifts in the Sloan Digital Sky Survey (Ahn et al. 2014), and many are part of the Cluster Infall Regions in SDSS project (CIRS; Rines & Diaferio 2006) or the Hectospec Cluster Survey (HeCS; Rines et al. 2013). To supplement this sample and create an SZ-selected sample of clusters, we conducted HeCS-SZ, an MMT/Hectospec spectroscopic survey of 24 clusters. We also include analysis of 30 clusters from SDSS redshifts.

We discuss the cluster samples and spectroscopic data in §2. We measure the SZ-optical scaling relations in §3. We discuss the implications of our results in the context of other cosmological observations in §4. We assume a cosmology of  $\Omega_m=0.3$ ,  $\Omega_\Lambda=0.7$ , and  $H_0=70$  km s<sup>-1</sup> Mpc<sup>-1</sup> for all calculations.

## 2. OBSERVATIONS

### 2.1. Optical Photometry and Spectroscopy

HeCS-SZ is an extension of the HeCS survey to include clusters that enable construction of an SZ-limited sample. We observed 7,721 new redshifts in 24 clusters. We combine these new measurements with the existing HeCS and CIRS surveys and with data from the literature to construct a total sample of 123 clusters. For all but a few clusters the sampling is sufficient for a robust determination of velocity dispersion. We use SDSS photometry for all clusters.

#### 2.1.1. Spectroscopy: CIRS and HeCS

The Hectospec Cluster Survey (HeCS) is a spectroscopic survey of 58 galaxy clusters at moderate redshift ( $z=0.1-0.3$ ) with MMT/Hectospec. HeCS includes all clusters with ROSAT X-ray fluxes of  $f_X > 5 \times 10^{-12}$  erg s<sup>-1</sup> at [0.5-2.0] keV from the Bright Cluster Survey (BCS; Ebeling et al. 1998) or REFLEX survey (Böhringer et al. 2004) with optical imaging in the Sixth Data Release (DR6) of SDSS (Adelman-McCarthy et al. 2008). We used DR6 photometry to select Hectospec targets. The HeCS targets are all brighter than  $r=20.8$  (SDSS cata-

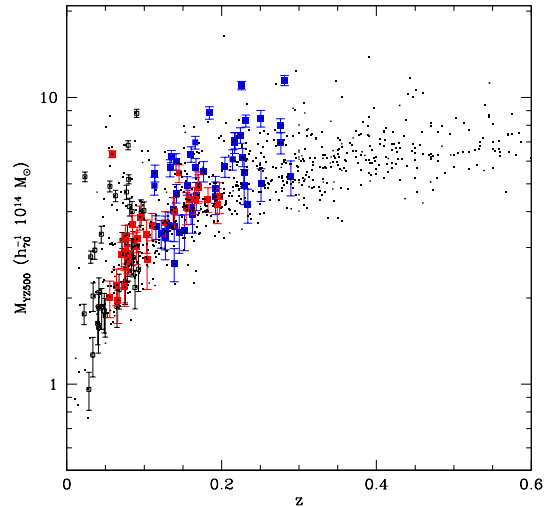


FIG. 1.— *Planck* SZ mass estimates versus redshift. Open black squares show clusters with dynamical mass estimates from CIRS. Solid blue and red squares show clusters from HeCS and new HeCS-SZ clusters respectively. Small points show the remainder of the *Planck* SZ catalog. The clusters studied here are representative of clusters at  $z < 0.3$  in the *Planck* SZ catalog.

logs are 95% complete for point sources to  $r \approx 22.2$ ).

For HeCS, we acquired spectra with the Hectospec instrument (Fabricant et al. 2005) on the MMT 6.5m telescope. Hectospec provides simultaneous spectroscopy of up to 300 objects across a diameter of 1°. This telescope and instrument combination is ideal for studying the virial regions and outskirts of clusters at these redshifts. Because cluster properties such as projected velocity dispersion depend on radius, wide-field spectroscopic coverage is important for measuring accurate global velocity dispersions and virial masses (Biviano et al. 2006). We used the red sequence to preselect likely cluster members as primary targets, and we filled otherwise unassigned fibers with bluer targets (Rines et al. 2013, describes the details of target selection).

CIRS used spectroscopy from the Fourth Data Release of SDSS to study the virial and infall regions of clusters. We use the dynamical data tabulated in CIRS for 25 clusters. We update dynamical parameters for two additional CIRS clusters: A2249 was poorly sampled in DR4 but has many more redshifts available in DR10. We use the DR10 redshifts to update the dynamical parameters. The central region of A2175 was poorly sampled in DR4. We thus obtained additional redshifts in the central parts of A2175 with Hectospec (see below).

#### 2.1.2. Spectroscopy: HeCS-SZ

We observed 24 clusters in the *Planck* catalog of SZ clusters using MMT/Hectospec. The target clusters are in the redshift range  $0.05 \leq z \leq 0.20$  and were observed mostly in decreasing *Planck* signal-to-noise ratio (a few clusters with relatively weak SZ signals were observed as backup targets for variable observing conditions). We also observed one field in A2175, a cluster from CIRS with limited SDSS spectroscopy in CIRS. Preliminary analysis indicated that A2175 had an unusually small velocity dispersion given its SZ mass. The additional redshifts in A2175 show that the CIRS data led to a

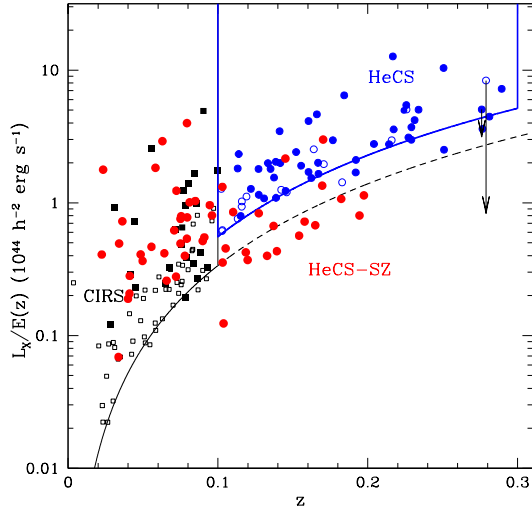


FIG. 2.— *ROSAT* X-ray luminosities of *Planck*-selected clusters versus redshift. Filled symbols are clusters in the HeCS-SZ sample: black squares show clusters with dynamical mass estimates from CIRS, blue points are clusters from HeCS, and red points are new clusters in HeCS-SZ.

significant underestimate of its velocity dispersion and caustic mass.

Our observing strategy closely matches that of HeCS: we used SDSS photometry to identify a red sequence in each cluster field. We then identify a cutoff in apparent magnitude that offers a good compromise of high completeness (sparser targets produce fewer fiber conflicts) and dense sampling. Targets are primarily drawn from galaxies with  $g - r$  colors within 0.2 mag of the red sequence, and we assign higher priorities to brighter galaxies and galaxies closer to the cluster center. This approach provides reasonably high sampling in the cluster cores but can lead to relatively sparse sampling of dense regions outside the core. We included galaxies with slightly bluer colors (up to 0.4 mag bluer than the red sequence) as targets to fill fibers when available. We matched all targets to redshifts from the literature as compiled by NED<sup>6</sup> as of 2013 September as well as to SDSS DR8 spectra. Most of the targets with existing redshifts are from SDSS, but several are from targeted studies of individual clusters (e.g., Cypriano et al. 2005, for A586). Targets with existing redshifts are removed from the targeting catalogs prior to fiber assignment.

Table 1 lists 7,721 new redshifts measured with Hectospec. We visually inspected all spectra to confirm the reliability of the redshift. Column 5 of Table 1 lists the cross-correlation score  $R_{XC}$  from the IRAF package *rvsao* (Kurtz & Mink 1998). A score of  $R_{XC} > 3$  indicates a reliable redshift; some galaxies with smaller values of  $R_{XC}$  are included when visual inspection shows multiple obvious absorption and/or emission lines and the spectrum suffers from contamination (e.g., light bleeding into the spectrum from a nearby fiber containing a bright star). Table 2 lists redshifts from SDSS and other literature (as compiled by NED) for galaxies classified as cluster members by the caustic technique (see below). Table 3 lists 168 redshifts measured with the FAST

<sup>6</sup> <http://ned.ipac.caltech.edu>

instrument (Fabricant et al. 1998) on the 1.5-meter Tillingham telescope at the Fred Lawrence Whipple Observatory. The additional single-slit spectra from FAST reduce the incompleteness of bright (SDSS  $r \lesssim 16.5$ ) galaxies in the HeCS-SZ clusters.

In addition, we identified several clusters in the *Planck* SZ catalog that lie below the completeness limits but that are at sufficiently low redshift ( $z \lesssim 0.1$ ) that they have reasonable redshift coverage in SDSS DR10. We include these clusters in an extended sample.

We include four nearby ( $z \leq 0.05$ ) clusters that lie inside the SDSS DR10 photometric footprint but outside the SDSS spectroscopic footprint. These nearby clusters have large numbers of redshifts available in the literature. Because of the redshift dependence of the limiting mass for SZ detection by *Planck* (driven by the large beam size of *Planck*), including these low-redshift clusters improves the sampling of low-mass clusters in the sample. The FAST redshifts in Table 3 are especially useful for these clusters.

Figure 1 shows the *Planck* SZ mass estimates versus redshift. The minimum mass a cluster must have to be detected by *Planck* increases with redshift because the SZ signal of lower-mass clusters at higher redshift is diluted by the large beam below the sensitivity of *Planck*.

The CIRS and HeCS clusters provide a good sampling of the  $M_{SZ} - z$  distribution, but this distribution is possibly biased due to the underlying X-ray selection of CIRS and HeCS. Figure 2 shows the X-ray luminosity of clusters in CIRS, HeCS, and HeCS-SZ as a function of redshift. The clusters we target with Hectospec include clusters that lie above the X-ray flux limits of CIRS and HeCS but were not in the appropriate SDSS photometric footprint and also clusters that have X-ray fluxes below the CIRS/HeCS flux limits. Targeting these X-ray-faint clusters enables a test of the impact of X-ray selection on the scaling relation parameters based on SZ and optical properties. The X-ray luminosities are measured in the ROSAT band but from heterogeneous sources (Ebeling et al. 1998; Böhringer et al. 2000, 2005; Piffaretti et al. 2011; *Planck* Collaboration et al. 2014b). A careful study of the X-ray properties of HeCS-SZ clusters would require a homogeneous reanalysis of ROSAT X-ray images.

TABLE 1  
HECS-SZ REDSHIFTS FROM MMT/HECTOSPEC

Coordinates (J2000)		$cz_{\odot}$	$\sigma_{cz}$	$R_{XC}$	Flag	Member
RA	DEC	km/s	km/s			
00:09:33.60	32:31:03.16	83460	52.19	6.23	Q	0
00:09:35.55	32:14:05.00	69478	182.17	1.64	Q	0
00:09:39.32	32:21:22.38	122251	49.89	5.08	Q	0
00:09:42.73	32:16:05.45	83482	100	4.45	Q	0
00:09:43.80	32:33:54.17	108270	9.69	15.29	Q	0

NOTE. — Table 1 is published in its entirety in the electronic edition of the Journal. A portion is shown here for guidance regarding its form and content.

The caustic technique (Diaferio 1999; Serra et al. 2011) uses a redshift-projected radius diagram to isolate cluster members from foreground and background galaxies in phase space. After smoothing the galaxy distribution in the redshift diagram, the infall regions of clusters produce well-defined envelopes containing the

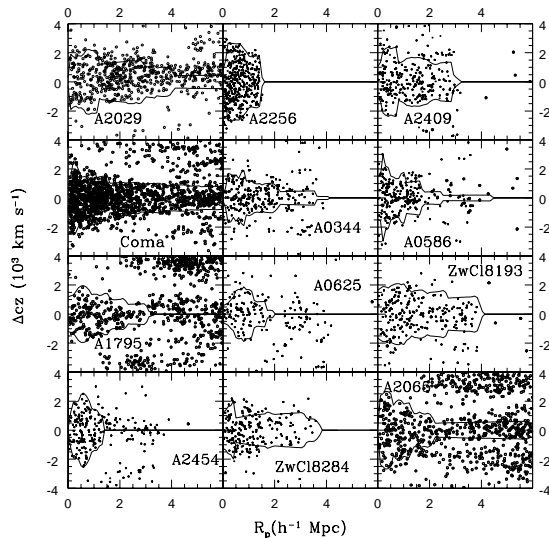


FIG. 3.— Redshift (rest-frame clustrocentric velocity) versus projected radius for galaxies around HECS-SZ clusters. The caustic pattern is evident as the trumpet-shaped regions with high density. The solid lines indicate our estimate of the location of the caustics in each cluster. Clusters are ordered left-to-right and top-to-bottom by decreasing mass as estimated from the *Planck* SZ data.

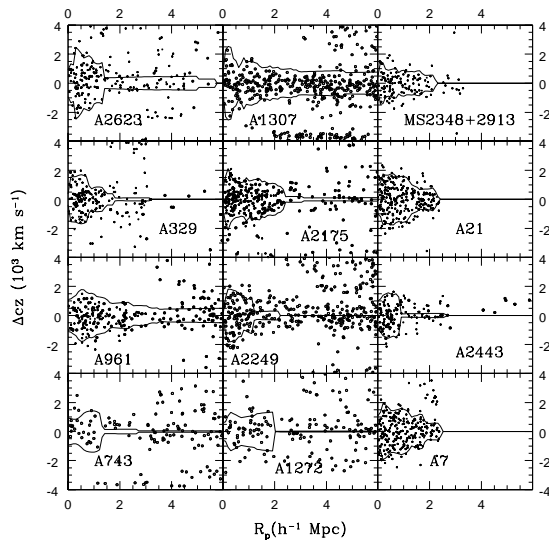


FIG. 4.— Same as Figure 3.

TABLE 2  
HECS-SZ MEMBERS FROM LITERATURE REDSHIFTS

Coordinates (J2000)		$cz_{\odot}$	$\sigma_{cz}$	Ref.
RA	DEC	km/s	km/s	
0:11:45.24	32:24:56.17	30309	100	2
0:11:19.72	32:17:09.39	32168	201	2
0:20:02.98	28:44:58.73	29876	27	2
0:20:05.48	28:41:01.73	29545	47	2
0:20:16.85	28:46:09.69	26793	33	2

NOTE. — Table 2 is published in its entirety in the electronic edition of the Journal. A portion is shown here for guidance regarding its form and content.

NOTE. — References: [1] SDSS, [2] NED.

vast majority of cluster members. Specifically, the

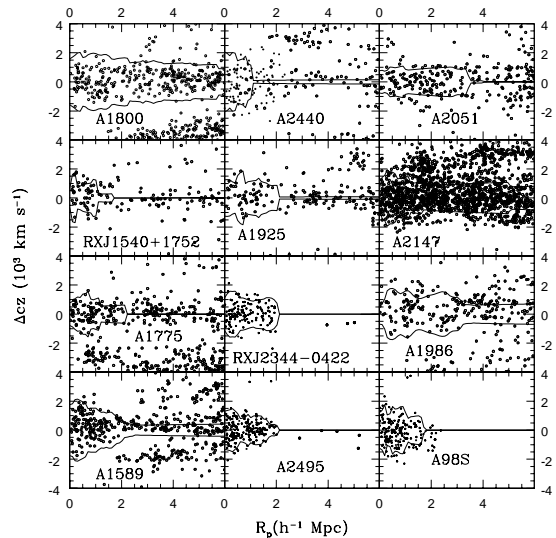


FIG. 5.— Same as Figure 3.

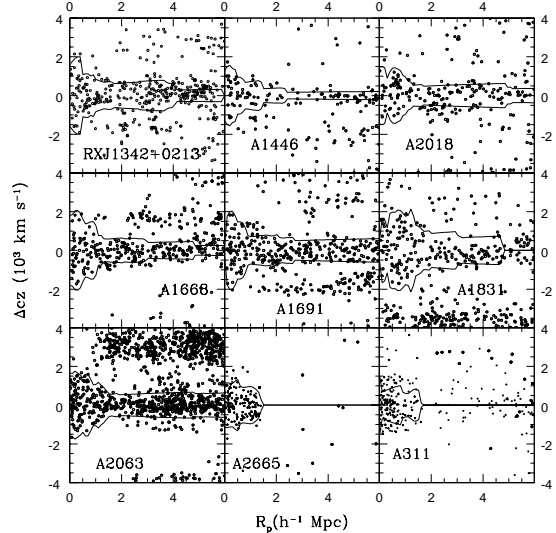


FIG. 6.— Same as Figure 3.

TABLE 3  
HECS-SZ REDSHIFTS FROM FLWO 1.5M/FAST

Coordinates (J2000)		$cz_{\odot}$	$\sigma_{cz}$	$R_{XC}$	Member
RA	DEC	km/s	km/s		
0:11:05.08	31:54:29.53	24574	24	9.01	0
0:11:34.79	32:28:16.28	30990	20	17.46	1
0:11:45.24	32:24:56.20	30542	51	6.47	1
0:12:27.58	32:45:09.84	12600	9	15.40	0
0:12:30.47	32:19:12.45	24565	5	31.67	0

NOTE. — Table 3 is published in its entirety in the electronic edition of the Journal. A portion is shown here for guidance regarding its form and content.

list of cluster members within  $r_{200}$  is 96% complete and only 2% of the members are actually interlopers; within the larger radius  $3r_{200}$ , where the caustic technique is the only usable method, the completeness is 95% and the interloper fraction is 8% (Serra & Diaferio 2013). The edges of this distribution are called caus-

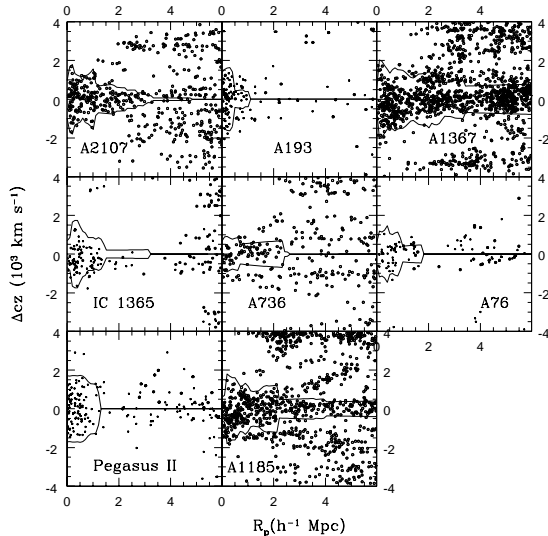


FIG. 7.— Same as Figure 3.

tics and they are related to the escape velocity profile of the cluster (see Diaferio 2009; Serra et al. 2011, for reviews). The escape velocity profile is the basis for a mass profile that can extend into the infall region where the galaxies are gravitationally bound but not virialized. Caustic mass estimates generally agree with estimates from X-ray observations and gravitational lensing (e.g., Rines et al. 2003; Biviano & Girardi 2003; Diaferio et al. 2005; Rines & Diaferio 2006; Rines et al. 2007; Geller et al. 2013, and references therein).

Figures 3-7 show the phase space diagrams of the HeCS-SZ clusters not already published in CIRS or HeCS (the poorly-sampled CIRS clusters A2175 and A2249 are reproduced here with enlarged datasets). Almost all clusters display prominent infall patterns, and the caustics are shown on the figures. Clusters are ordered by decreasing SZ mass, and there is a clear trend of decreasing central velocity dispersion with decreasing SZ mass.

We apply the prescription of Danese et al. (1980) to determine the mean redshift  $cz_{\odot}$  and projected velocity dispersion  $\sigma_p$  of each cluster from all galaxies within the caustics. We calculate  $\sigma_p$  using only the cluster members projected within  $r_{200}$  estimated from the caustic mass profile. Note that our measured velocity dispersions use the caustic technique only to define membership and the limiting radius  $r_{200}$ . Independent of its performance as a mass estimator, the caustic technique is a highly efficient membership selection algorithm, especially at the relatively small radii we focus on here (Serra & Diaferio 2013). Table 4 lists the central cluster redshifts, velocity dispersions inside  $r_{200}$ , and  $M_{200}$  from the caustic mass profile. The ninth column of Table 4 indicates whether the cluster is part of the CIRS, HeCS, or HeCS-SZ sample.

## 2.2. SZ Measurements

The SZ measurements are from Planck Collaboration et al. (2014b), an all-sky SZ survey. Numerical simulations indicate that the integrated Compton  $y$ -parameter  $Y_{SZ}$  has smaller scatter than the peak  $y$ -decrement  $y_{peak}$  (Motl et al. 2005; Planck Collaboration et al. 2014b).

Planck Collaboration et al. (2014b) report only  $Y_{SZ}$ . Although  $y_{peak}$  should be nearly independent of redshift,  $Y_{SZ}$  depends on the angular size of the cluster. The quantity  $Y_{SZ}D_A^2$  removes this dependence. Table 4 summarizes the *Planck* SZ measurements.

The *Planck* mass estimates are extracted from an aperture of  $\theta_{500}$ , the angular radius corresponding to  $r_{500}$  (the radius  $r_{\Delta}$  is the radius that encloses a mean density of  $\Delta\rho_c(z)$  where  $\rho_c(z)$  is the critical density). This radius is larger than the radii probed by some other mass estimators. For instance, Bonamente et al. (2008) and Mantz et al. (2010a) find that X-ray masses are best determined within  $r_{2500}$  (although Vikhlinin et al. 2009a, and others use  $M_{500}$ ). Marrone et al. (2009) uses an aperture of 350 kpc as the best match to their mass estimates from strong gravitational lensing. Because the SZ signal falls off more slowly with radius than the X-ray flux, the outer parts of clusters are more important for SZ observables than for X-ray observables. For instance, Planck Collaboration et al. (2013b) used *Planck* data to determine the average pressure profile of the ICM to radii of  $3r_{500}$ , a regime that is very difficult to study even with very deep *Chandra* observations. Because virial masses and velocity dispersions are best suited for mass estimates at radii  $\sim r_{200}$ , they may be better suited for comparison with SZ mass estimates.

The central redshifts in the *Planck* SZ catalog are usually close to the central redshifts we obtain in our hierarchical clustering analysis of the cluster redshifts (see D99 for details). However, for about half of the clusters, our central redshifts differs by more than a percent from the redshifts listed in the *Planck* SZ catalog. We therefore re-scale all SZ integrated Compton parameters by  $[D_A^2(z_h)/D_A^2(z_{SZ})]$  where  $D_A(z_h)$  and  $D_A(z_{SZ})$  are the angular diameter distances for the hierarchical center  $z_h$  and the *Planck* catalog redshift  $z_{SZ}$ . We similarly rescale SZ mass estimates using the appropriate scaling relation from Planck Collaboration et al. (2014b).

We define an SZ-complete sample of 83 clusters from the SZ mass proxy  $M_{500}$  in the *Planck* SZ catalog. The final column of Table 4 indicates whether the cluster is in the complete sample. The completeness limit corresponds to the 80% completeness limit for the medium-deep survey covering 44% of the sky and to the 50% completeness limit for the shallow survey covering the remaining 56% of the sky (Planck Collaboration et al. 2014b). Our sample includes all but four clusters above this limit: two at moderate redshift (A1677 at  $z=0.18$  and A1759 at  $z=0.17$ ) and two at low redshift ( $z \approx 0.04$ : A2572 and RBS 1929). The SZ completeness limits we use are slightly above the 80% completeness limits of the updated *Planck* SZ catalog (Planck Collaboration et al. 2015b). A quick inspection shows that the updated SZ catalog contains few clusters above the completeness limits we use here.

## 3. RESULTS

As discussed in §1, data from the *Planck* satellite indicate tension between cosmological parameters determined from CMB and SZ results. One possible resolution to the tension is that the SZ mass estimates (calibrated with hydrostatic X-ray mass estimates) are biased. Comparing dynamical estimates of cluster mass from galaxy redshift surveys to the

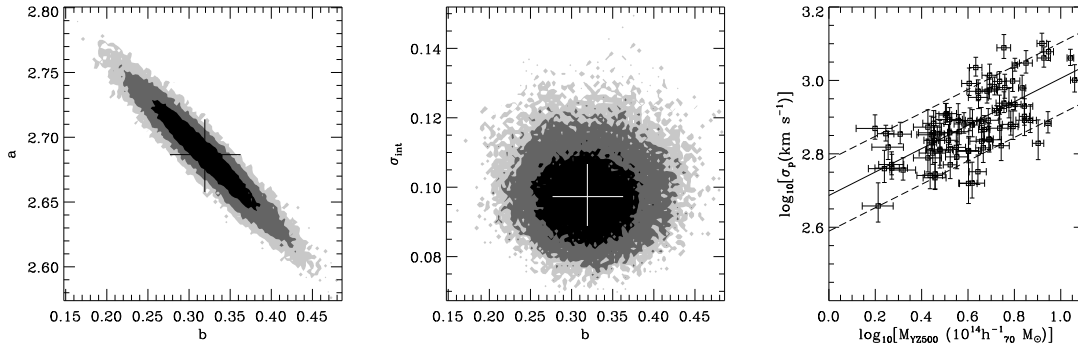


FIG. 8.— Scaling relation between projected velocity dispersion  $\sigma_p$  and  $M_{SZ}$ , the mass proxy based on the integrated Compton parameter  $Y_{SZ}$ . The first two panels show the marginalized probability distribution functions of the parameters  $a$  (intercept),  $b$  (slope), and  $\sigma_{int}$  (the intrinsic scatter). The first panel shows that the slope and intercept are correlated. Shaded regions indicate 68%, 95%, and 99% confidence regions from darkest to lightest shading. The crosses show the median and the 68% confidence range of the probability distribution functions. The third panel shows the relation with the median values of  $a$  and  $b$  as a solid line with the median value of the intrinsic scatter  $\sigma_{int}$  shown by the dashed lines.

TABLE 4  
DYNAMICAL MASSES AND SZ SIGNALS

Cluster	$\alpha$ deg	$\delta$ deg	$z$	$\sigma_p$ km s $^{-1}$	$M_{200,c}$ $10^{14} M_\odot$	$M_{SZ}$ $10^{14} M_\odot$	$Y_{SZ} D_A^2$ $10^{-5} \text{Mpc}^{-2}$	Spectra	<i>Planck</i> ID	Sample
A0007	2.93500	32.41700	0.10302	$783^{+58}_{-48}$	$2.77 \pm 1.14$	$3.317^{+0.420}_{-0.456}$	$0.105^{+0.025}_{-0.024}$	HeCS-SZ	PSZ1G113.26-29.69	1
A0021	5.17050	28.67510	0.09456	$761^{+54}_{-44}$	$2.92 \pm 1.33$	$3.825^{+0.359}_{-0.379}$	$0.146^{+0.025}_{-0.025}$	HeCS-SZ	PSZ1G114.78-33.72	1
A0076	10.00200	6.81800	0.03999	$455^{+66}_{-46}$	$1.19 \pm 0.04$	$1.631^{+0.243}_{-0.258}$	$0.032^{+0.003}_{-0.008}$	HeCS-SZ	PSZ1G118.03-55.88	1
A0085	10.45870	-9.30190	0.05565	$692^{+55}_{-45}$	$2.50 \pm 1.19$	$4.900^{+0.213}_{-0.217}$	$0.225^{+0.018}_{-0.018}$	CIRS	PSZ1G115.20-72.07	1
A0098S	11.61470	20.38645	0.10380	$594^{+48}_{-39}$	$2.17 \pm 0.09$	$2.733^{+0.516}_{-0.591}$	$0.079^{+0.029}_{-0.028}$	HeCS-SZ	PSZ1G121.35-42.47	0

NOTE. — Table 4 is published in its entirety in the electronic edition of the Journal. A portion is shown here for guidance regarding its form and content.

NOTE. — Redshift  $z$  and velocity dispersion  $\sigma_p$  are computed for galaxies defined as members using the caustics.

SZ mass proxies tests this hypothesis. Several studies show a strong correlation between X-ray mass estimates and SZ mass estimates (e.g., Bonamente et al. 2008; Andersson et al. 2011; Planck Collaboration et al. 2011; Czakon et al. 2015), but both methods measure the properties of the intracluster medium (ICM). Thus, systematic effects could still be present. For instance, the ICM is likely to depart from hydrostatic equilibrium in the outer parts of the cluster (Bonamente et al. 2013). Gravitational lensing does not measure the ICM, but it does measure all of the matter along the line of sight to the cluster, introducing significant scatter into lensing mass estimates (e.g., Hoekstra et al. 2001, 2011; Hwang et al. 2014). Marrone et al. (2009) show that lensing masses are consistent with SZ estimates although with significant scatter. Recently, von der Linden et al. (2014) and Hoekstra et al. (2015) have used large samples of weak lensing mass estimates to test for systematic bias in SZ masses; both groups find that the SZ masses are systematically underestimated, but both estimates of bias are smaller than the value required to fully reconcile *Planck* CMB and SZ results (the uncertainty range in bias obtained by von der Linden et al. 2014, includes this value within the  $2\sigma$  confidence interval). In contrast, Melin & Bartlett (2014) use weak lensing of the CMB to estimate cluster masses, and they find little evidence for mass bias.

Figure 8 shows the relation between projected velocity dispersion  $\sigma_p$  and the mass  $M_{SZ}$  estimated from the

*Planck* data (note that, for most clusters, the measurements of  $Y_{SZ}$  use X-ray data to determine the region where the SZ signal is extracted). We use a Bayesian approach (see Appendix for details) to determine the best-fit relation  $P(\sigma_p|M_{SZ})$ , that is, the predicted value of  $\sigma_p$  at a given observed value of  $M_{SZ}$ . We allow for intrinsic scatter in  $\sigma_p$  that is expected to arise from projection effects of non-spherical clusters. Our Bayesian analysis yields a relation of

$$\log_{10}(\sigma_p) = 0.319^{+0.043}_{-0.042} \log_{10}(M_{SZ}) + 2.687^{+0.027}_{-0.029} \quad (1)$$

with  $\sigma_p$  in units of km s $^{-1}$  and  $M_{SZ}$  in units of  $10^{14} h_{70}^{-1} M_\odot$ . The scatter in  $\sigma_p$  at fixed  $M_{SZ}$  is  $\log_{10} \sigma = 0.0973^{+0.0094}_{-0.0085}$ . The best-fit parameters and their uncertainties are the medians and the boundaries of the 68% confidence levels derived from the posterior probability of the regression parameters. Figure 8 shows this relation as a solid line. Note that we fit  $P(\sigma_p|M_{SZ})$  rather than the inverse because the statistical uncertainties in  $M_{SZ}$  are smaller than the statistical uncertainties in  $\sigma_p$ .

The intrinsic scatter we measure corresponds to about a factor of two in the estimated mass within  $r_{200}$ . A comparison of several richness-based and dynamics-based mass estimators demonstrate similar scatter for several mass estimators based on velocity dispersions or variations of Jeans' analysis (Old et al. 2013). Thus, the scatter probably represents geometric projection effects and not our use of the caustic technique to define cluster

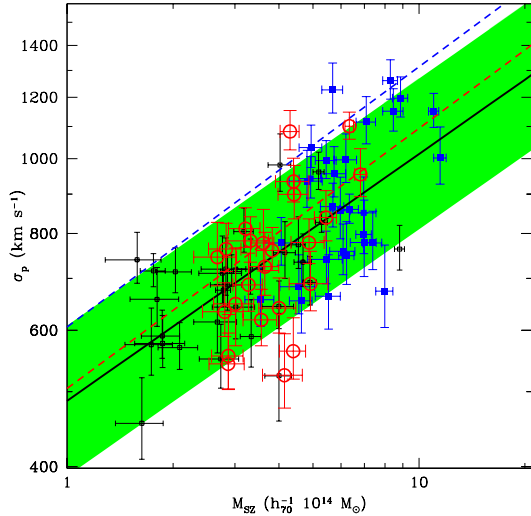


FIG. 9.— Scaling relation between projected velocity dispersion  $\sigma_p$  and the SZ mass proxy  $M_{SZ}$  based on the integrated Compton parameter  $Y_{500}D_A^2$ . The thick solid line shows the best-fit relation of  $P(\sigma_p|M_{SZ})$  with the intrinsic scatter shown as the green band. Open squares, filled squares, and open circles represent clusters from CIRS, HeCS, and HeCS-SZ respectively. The dotted line shows the relation from Rines et al. (2010) from a small number of clusters. The red dashed line shows the predicted relation using the virial scaling relation from Evrard et al. (2008) and assuming no hydrostatic mass bias (i.e.,  $1-b=0$ ). The blue dashed line shows the same predicted relation for the bias ( $1-b=0.58$ ) required to reconcile *Planck* SZ counts with the *Planck* CMB cosmology.

membership.

Previous work provides an expected value for this slope. Numerical simulations of clusters with a variety of codes yield a consistent scaling relation of the mass  $M_{200}$  with velocity dispersion,  $\sigma_p \propto M_{200}^{0.33}$  (Evrard et al. 2008). This slope is measured for randomly selected dark matter particles rather than galaxies, but hydrodynamical simulations suggest that velocity bias is small for large samples of cluster galaxies (Wu et al. 2013) like HeCS and CIRS (we discuss velocity bias further in §4.4). The slope of the scaling relation for dark matter particles in clusters agrees well with our observed  $\sigma_p - M_{SZ}$  relation (Equation 1). Figure 9 shows our data and scaling relation compared to the virial scaling of dark matter particles, and the agreement is reasonable. Figure 10 shows the marginalized probability distribution functions of the parameters of our scaling relation along with the virial scaling of dark matter particles. Figures 9 and 10 also show the virial scaling of dark matter particles rescaled by assuming that  $M_{SZ} = 0.58M_{true}$ , the mass bias required to match the SZ counts to the CMB data. Such a large mass bias is strongly disfavored by our observations.

Figure 11 shows the best-fit relation for  $P(\sigma_p|Y_{SZ}D_A^2)$ , the expected velocity dispersion at fixed SZ mass proxy  $Y_{SZ}D_A^2$ . Planck Collaboration et al. (2014b) obtain  $M_{500}^{1.79} \propto (Y_{SZ}D_A^2)$  using hydrostatic mass estimates from detailed XMM-Newton observations. Because the concentration-mass relation depends weakly on mass (e.g., Bullock et al. 2001), we use a fixed conversion of  $M_{200} \approx 1.35M_{500}$  appropriate for concentration  $c=5$  assuming an NFW profile (Navarro et al. 1997). With these assumptions, the expected slope of the  $\sigma_p - Y_{SZ}$

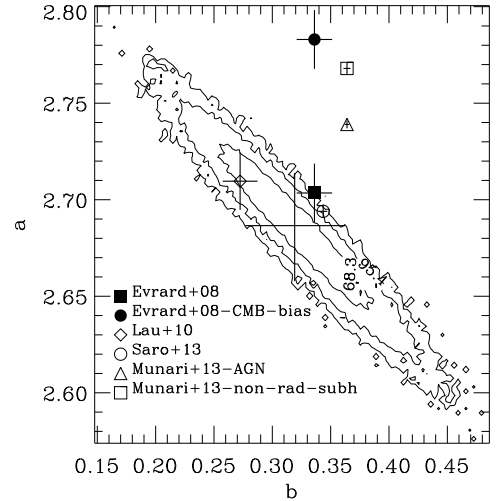


FIG. 10.— Parameters of the virial scaling relation between projected velocity dispersion  $\sigma_p$  and the SZ mass proxy  $M_{SZ}$  based on the integrated Compton parameter  $Y_{500}D_A^2$  ( $a$  is the intercept,  $b$  is the slope). Contours show confidence intervals from our Bayesian analysis and the cross without a symbol shows the median and 68% percentiles of the distribution shown with the contour levels. Points with errorbars show models based on simulations. The filled square is the virial scaling relation of dark matter particles from Evrard et al. (2008). The filled circle shows this same relation renormalized to reflect a mass bias of  $M_{SZ} = 0.59M_{true}$ , the value needed to match SZ and CMB constraints. The other points show several models of velocity bias. The open triangle and open square show the models of Munari et al. (2013) for galaxies identified from dark matter subhalos and from hydrodynamical simulations including star formation and AGN feedback. The open diamond shows the model of Lau et al. (2010), and the open circle shows the model of Saro et al. (2013).

relation is 0.188 with an intercept of 3.003. Figure 11 shows that these values agree very well with our Bayesian analysis (see also Table 5).

In contrast with our previous work (Rines et al. 2010), the relation between projected velocity dispersion  $\sigma_p$  and  $Y_{SZ}D_A^2$  agrees with expectations from scaling relations of dark matter particles and simulations of the SZ effect. We attribute this difference to both the much larger (5x) sample of clusters studied here and the improved statistical methods enabled by the larger sample.

Figure 12 shows the best-fit relation  $P(M_{200}|M_{SZ})$ , the caustic mass  $M_{200}$  obtained at fixed  $M_{SZ}$ . The intrinsic scatter in this relation is somewhat smaller than a factor of two, consistent with the expected scatter in caustic mass estimates due to projection effects (Serra et al. 2011). Note that a similar level of scatter is found for alternate implementations of the caustic technique (Gifford & Miller 2013) as well as alternative mass estimators based on measured velocity dispersions (Old et al. 2014). While a detailed treatment of outliers is beyond the scope of this work, we note that one cluster, MS2348+2929, with an observed velocity dispersion smaller than predicted by its *Planck* SZ mass, is undetected in observations with the Arcminute Microkelvin Imager (Perrott et al. 2014), suggesting that the SZ mass in the *Planck* catalog is an overestimate.

Figure 13 shows the  $\sigma_p - M_{SZ}$  relation for the extended sample of 123 clusters. There are significantly more outliers than in the SZ-complete sample. Most of these out-

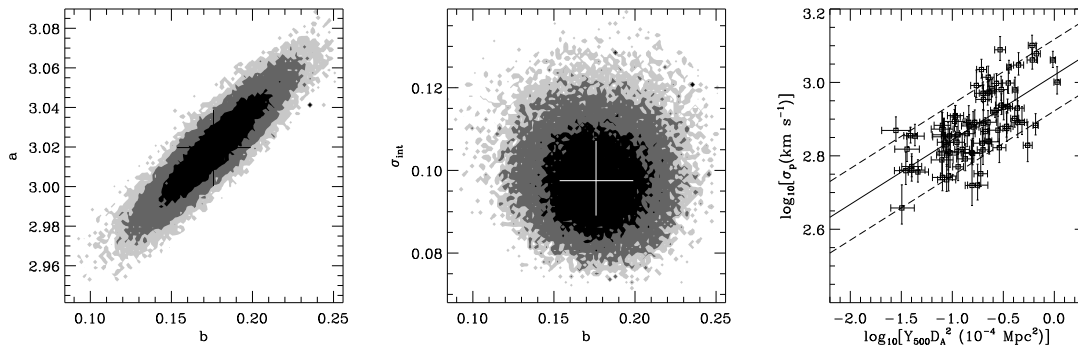


FIG. 11.— Similar to Figure 8 for the scaling relation between projected velocity dispersion  $\sigma_p$  and the integrated Compton parameter  $Y_{SZ}$ .

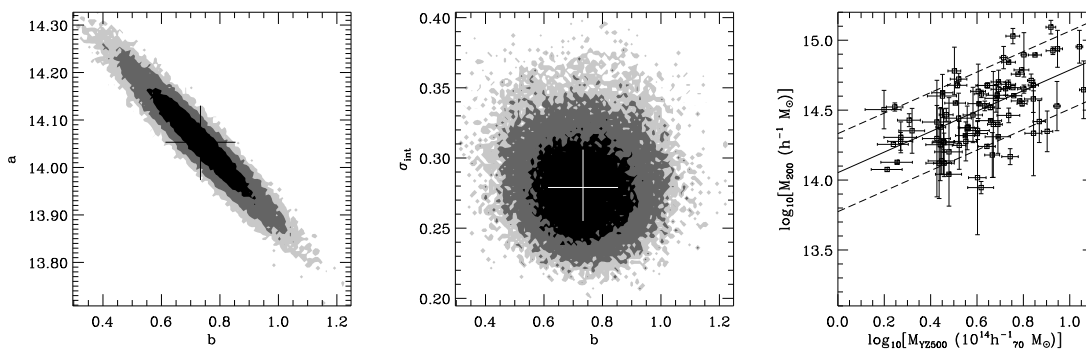


FIG. 12.— Similar to Figure 8 for the scaling relation between caustic mass  $M_{200}$  and  $M_{SZ}$ , the mass proxy based on the integrated Compton parameter  $Y_{SZ}$ .

liers have redshifts only from SDSS, and some are at  $z > 0.1$ . Thus, these clusters are not well sampled. Obtaining additional redshifts for these clusters could significantly alter the measured velocity dispersions (similar to the changes for the CIRS clusters A2175 and A2249 resulting from additional redshift data from Hectospec and SDSS respectively). The best-fit parameters of the scaling relation are virtually unchanged, but the inferred intrinsic scatter is larger due to the larger number of outliers (Table 5).

#### 4. DISCUSSION

##### 4.1. Predictor Relations

Cluster scaling relations applied to large surveys are a basis for cosmological studies, including measuring the cluster mass function or the power spectrum (Mantz et al. 2010b; Rozo et al. 2010). Andreon (2010) discusses how, given observable properties A and B, the slopes of the predictor relation  $P(A|B)$  (the probability of a cluster having the property A given an observed value of property B) may be significantly different from the inverse of the slope of the predictor relation  $P(B|A)$ . This difference is larger when there is significant intrinsic scatter in the relation between the two properties.

Because different investigators require different predictor relations, we include here the relations between several mass observables (Table 5). We do not include constraints on the  $M_{SZ} - M_{200}$  relation for the extended sample because the large scatter caused by a few outliers leads to very weak constraints on the parameters of the

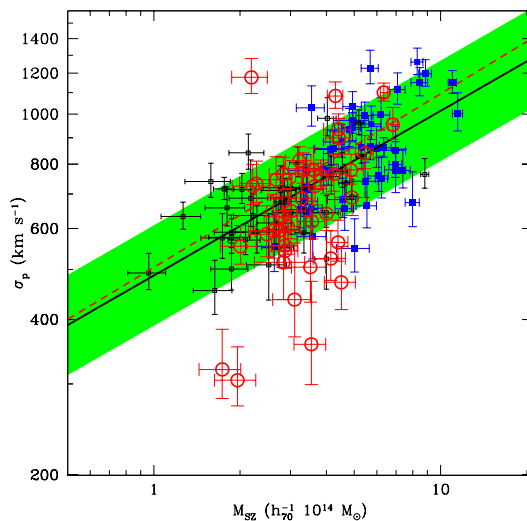


FIG. 13.— Scaling relation between projected velocity dispersion  $\sigma_p$  and the SZ mass proxy  $M_{SZ}$  based on the integrated Compton parameter  $Y_{500}D_A^2$  for the extended sample of *Planck*-selected clusters (including clusters below the *Planck* completeness limits). Several clusters in the extended sample are outliers below the main relation. These clusters are not well sampled in SDSS spectroscopy, so their velocity dispersions are likely underestimated.

scaling relation.



TABLE 5  
SCALING RELATIONS BETWEEN DYNAMICAL MASSES AND SZ SIGNALS

Relation	$b$	$a$	$\sigma_y$
$P(\sigma_p Y_{500}D_A^2)$	$0.176^{+0.023}_{-0.022}$	$3.020^{+0.019}_{-0.019}$	$0.0975^{+0.0096}_{-0.0084}$
extended sample	$0.191^{+0.022}_{-0.022}$	$3.023^{+0.021}_{-0.021}$	$0.1182^{+0.0096}_{-0.0088}$
CIRS/HeCS	$0.175^{+0.029}_{-0.030}$	$3.013^{+0.024}_{-0.024}$	$0.114^{+0.012}_{-0.010}$
$P(Y_{500}D_A^2 \sigma_p)$	$2.36^{+0.31}_{-0.29}$	$-7.57^{+0.83}_{-0.91}$	$0.371^{+0.035}_{-0.031}$
extended sample	$2.02^{+0.29}_{-0.26}$	$-6.63^{+0.75}_{-0.83}$	$0.394^{+0.029}_{-0.026}$
$P(M_{200} M_{SZ})$	$0.73^{+0.12}_{-0.12}$	$14.053^{+0.077}_{-0.080}$	$0.279^{+0.027}_{-0.024}$
extended sample	$0.76^{+0.12}_{-0.12}$	$14.006^{+0.071}_{-0.071}$	$0.346^{+0.027}_{-0.024}$
CIRS/HeCS	$0.70^{+0.15}_{-0.15}$	$14.069^{+0.099}_{-0.096}$	$0.308^{+0.034}_{-0.029}$
$P(M_{SZ} M_{200})$	$1.72^{+0.57}_{-0.79}$	$-24.2^{+11.5}_{-8.3}$	$0.46^{+0.26}_{-0.19}$
$P(\sigma_p M_{SZ})$	$0.319^{+0.043}_{-0.041}$	$2.687^{+0.027}_{-0.029}$	$0.0973^{+0.0094}_{-0.0085}$
extended sample	$0.339^{+0.043}_{-0.041}$	$2.665^{+0.025}_{-0.026}$	$0.1198^{+0.0096}_{-0.0087}$
$P(M_{SZ} \sigma_p)$	$1.42^{+0.16}_{-0.19}$	$-3.47^{+0.55}_{-0.46}$	$0.205^{+0.019}_{-0.017}$
extended sample	$1.03^{+0.19}_{-0.09}$	$-2.36^{+0.26}_{-0.34}$	$0.222^{+0.017}_{-0.015}$

NOTE. — Fits are of the relation  $P(y|x)$  assuming the linear form  $\log y = a + b \log x$  with intrinsic scatter  $\sigma_{\log y}$  in the relation at fixed values of  $\log x$ .

#### 4.2. Impact on the Tension Between Planck Cosmological Parameters from SZ versus CMB

Cosmological constraints from *Planck* observations of the CMB predict a higher normalization of the cluster mass function (parameterized by  $\Omega_m$  and  $\sigma_8$ ) than the measured abundance from the SZ cluster detections (Planck Collaboration et al. 2014a). As discussed in that paper, the cluster constraints are based on a scaling relation between SZ integrated Compton decrement and X-ray masses (calculated with the assumption of hydrostatic equilibrium). They assume a hydrostatic mass bias due to non-thermal pressure support parameterized as  $M_{true} = (1 - b)M_{HSE}$  where  $M_{true}$  and  $M_{HSE}$  are respectively the true cluster mass and the mass estimated under the assumption of hydrostatic equilibrium. Hydrodynamic simulations of intracluster gas (Nagai et al. 2007; Nelson et al. 2014) predict a value of  $(1 - b) = 0.8$ , and the cosmological constraints are derived by allowing this parameter to vary in the range  $0 < b < 0.3$ . The tension between the SZ and CMB constraints can be eliminated by assuming that the hydrostatic mass bias is significantly larger,  $(1 - b) = 0.58 \pm 0.04$  (Planck Collaboration et al. 2014a, 2015a). Note that the parameter  $b$  can have non-zero values either because of non-thermal pressure support or because of other calibration offsets (e.g., XMM-Newton temperature calibration, see Israel et al. 2015; Schellenberger et al. 2015).

Estimates of hydrostatic mass bias from comparisons of X-ray and lensing mass estimates find smaller offsets (e.g., Vikhlinin et al. 2009a; Mahdavi et al. 2013; Applegate et al. 2014). Recent revisions to systematic uncertainties in lensing mass estimates yield consistency in mass estimates of individual clusters between different investigators (von der Linden et al. 2014; Hoekstra et al. 2015), yielding estimates of  $(1 - b) \approx 0.7 - 0.8$ , intermediate between no hydrostatic mass bias and the large bias required to match CMB constraints. Alternatively, a new method of measuring weak lensing of the CMB by clusters yields  $1/(1 - b) = 0.99 \pm 0.19$ , consistent with little to no mass bias (Melin & Bartlett 2014).

It is thus very interesting to see whether our dynamical mass estimates imply small hydrostatic mass bias (leav-

ing tension between clusters and the CMB) or large hydrostatic mass bias (alleviating tension between clusters and the CMB but aggravating tension among different cluster mass estimators). As mentioned in §3, our best-fit scaling relation is consistent with the *Planck* scaling relation based on hydrostatic mass estimates from XMM-Newton observations. Furthermore, Figure 9 shows that renormalizing this relation by assuming a hydrostatic mass bias of  $(1 - b) = 0.58 \pm 0.04$  overpredicts the velocity dispersion at fixed  $Y_{SZ}$  by an amount larger than the statistical uncertainties. That is, the CMB cosmological parameters predict significantly larger cluster velocity dispersions than our measured values.

We next consider three possible explanations of the tension between the CMB normalization of the cluster mass scale and our measurement of the relation between velocity dispersion and integrated SZ decrement. First, we investigate whether X-ray selection (used for part of the sample at larger redshift) significantly impacts the resulting scaling relation. Second, we discuss the possibility of velocity bias (galaxies moving faster or slower than dark matter particles). Third, we discuss the possible impact of massive neutrinos producing a smaller cluster abundance for a fixed matter power spectrum.

#### 4.3. Impact of Cluster Selection

Scaling relations can be sensitive to the method of sample selection. The relation between dynamical mass and SZ signal could depend on whether the cluster sample is selected from an optical catalog, an X-ray catalog, or a SZ catalog, and whether the samples are flux-limited (detection-limited) or volume-limited. For instance, clusters with luminous cooling cores could be overrepresented in a flux-limited X-ray catalog compared to a mass-limited sample. The HeCS and CIRS cluster samples were drawn from X-ray-selected samples. Thus, all clusters from these samples have moderately large X-ray fluxes. The *Planck* early release clusters contained several that were not previously detected in X-rays. Followup *XMM-Newton* observations of these clusters showed that they are in younger dynamical states than the rest of the early release clusters (Planck Collaboration et al. 2013a). Thus, it is conceiv-

able that the HeCS and CIRS clusters are not a representative sample of *Planck* clusters.

We use our *Planck*-selected sample to test whether the scaling relations depend on the selection technique. Specifically, we fit the scaling relations based on only clusters from the CIRS and HeCS samples, both of which are selected by X-ray flux. There is no significant change in the best-fit parameters for the X-ray selected sample compared to the SZ-selected sample (Table 5<sup>7</sup>). Thus, the impact of X-ray selection versus SZ selection appears to be small, at least for the large and complete samples that we consider here.

#### 4.4. Can Velocity Bias Resolve the Tension?

In numerical simulations, the velocity dispersion of randomly selected dark matter particles closely traces the mass of dark matter halos (Evrard et al. 2008). Observationally, one measures the velocity dispersion of galaxies, which may move faster or slower than the underlying dark matter distribution. This “velocity bias” can be parametrized as  $b_v = \sigma_{gxy}/\sigma_{DM}$ , where  $\sigma_{gxy}$  and  $\sigma_{DM}$  are the velocity dispersions of galaxies and dark matter particles respectively.

If one assumes that the *Planck* CMB cosmological parameters are correct, then the offset between the scaling relation we observe and the relation predicted by the CMB-based parameters provides information about the relation between galaxy dynamics and true cluster mass. In particular, significant negative velocity bias ( $b_v \approx 0.77$ ) is required to bring the results into agreement.

Modeling velocity bias in simulations is a very challenging problem, due to both the uncertain physics in galaxy formation and evolution and the large dynamic range required to simulate individual cluster galaxies in a cosmological simulation. Some simulations follow the evolution of dark matter subhalos, but the evolution of galaxies may differ significantly because galaxies are expected to form at the centers of dark matter subhalos and thus survive even after their dark matter halos are tidally stripped.

Earlier, we used the consistency of the virial mass function of X-ray selected clusters with cosmological constraints from WMAP5, supernovae, and baryon acoustic oscillations to conclude that velocity bias is small:  $\sigma_{gxy} = (1.05 \pm 0.05)\sigma_{DM}$  (Rines et al. 2008). At present, there is no general agreement on the amount or even the sign of velocity bias, but the large negative velocity bias required for consistency with *Planck* CMB-based parameters is not predicted by any current models. Simulations suggest that small samples of cluster galaxies restricted only to the brightest members could be subject to negative velocity bias of  $\sim 15\%$  (Old et al. 2013; Wu et al. 2013), but these simulations also suggest that large samples such as the ones we analyze here should not be subject to significant velocity bias.

Note that a recent analysis of the redshift-space correlation function of high-mass galaxies from the SDSS Baryon Oscillation Spectroscopic Survey (BOSS) suggests that  $b_v \approx 0.86$  (Guo et al. 2015). This negative

velocity bias probably reflects the fact that even massive and rich clusters contain very few high-mass galaxies (e.g., Figure 4 of Guo et al. 2015); thus, the measured velocity bias is consistent with simulations that predict negative velocity bias for the brightest few galaxies (Old et al. 2013; Wu et al. 2013). It is also possible that the analysis of Guo et al. (2015) does not adequately model the impact of coherent infall among satellite galaxies (Hikage & Yamamoto 2015). Again, the spectroscopic samples considered here include many galaxies below the characteristic absolute magnitude  $M_*$  and are thus expected to have smaller bias than more luminous samples.

Several recent simulations suggest that cluster galaxies should be positively biased by 5-15% depending on the details of galaxy modeling (Lau et al. 2010; Saro et al. 2013; Munari et al. 2013). Positive velocity bias would further aggravate the tension between the velocity dispersions we measure and the large SZ-mass normalization required to match the CMB data.

Many of the simulations predict that the velocity bias depends weakly on halo mass, so a more complete description of velocity bias may require a virial scaling relation with arbitrary slope (fixed  $b_v$  requires that the slope of the  $\sigma_{gxy} - M$  relation is identical to the  $\sigma_{DM} - M$  relation). Figure 14 shows several of these relations compared to our data, and Figure 10 shows the parameters of some of these models compared to the uncertainties in our observed scaling relation. The HeCS-SZ data and *Planck* masses are consistent with the models of Lau et al. (2010), while the models of Munari et al. (2013) lie far outside the observed relation. Importantly, although there is no consensus on the exact amount of velocity bias, none of the recent estimates are consistent with the large velocity bias ( $b_v \sim 0.77$ ) required to reconcile the *Planck* SZ mass function with the CMB. Indeed, the discrepancy between our observed scaling relation and the models of Munari et al. (2013) is in the opposite direction of the discrepancy required to reduce the CMB-SZ tension.

#### 4.5. Massive Neutrinos as a Solution?

Neutrinos with significant masses can suppress the formation of large-scale structure. Thus, massive neutrinos provide one possible explanation of the observed deficit of SZ clusters compared to the predictions from the best-fit  $\Lambda$ CDM model to the *Planck* CMB data. In particular, joint fits to CMB and SZ data from *Planck* yield estimates of total neutrino masses  $\Sigma m_\nu = (0.40 \pm 0.21)\text{eV}$  when allowing the hydrostatic mass bias to vary between 0 and 0.3 (Planck Collaboration et al. 2014a). Adding baryon acoustic oscillation (BAO) measurements yields an estimate of  $\Sigma m_\nu = (0.20 \pm 0.09)\text{eV}$  (Planck Collaboration et al. 2014a). Wyman et al. (2014) point out that massive neutrinos not only alleviate tension between *Planck* CMB results and cluster abundance measurements, they also alleviate tension between *Planck* CMB results and local measurements of the Hubble constant. Similarly, MacCrann et al. (2015) find that a similar tension exists between *Planck* CMB results and cosmic shear measurements; this tension can be partially alleviated with the introduction of a sterile neutrino. However, note that an alternate analysis of the cluster mass function using X-ray luminosities and weak lensing

<sup>7</sup> Because  $M_{SZ}$  and  $Y_{SZ}D_A^2$  are closely related, we do not include a separate fit for the  $\sigma_p - M_{SZ}$  relation for the CIRS/HeCS subsample.

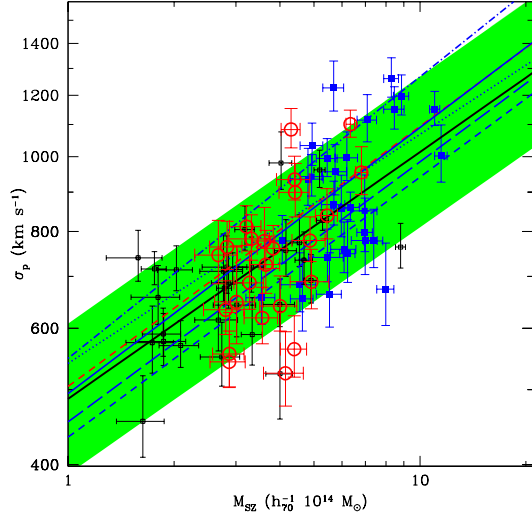


FIG. 14.— Scaling relation between projected velocity dispersion  $\sigma_p$  and the SZ mass proxy  $M_{SZ}$  based on the integrated Compton parameter  $Y_{500} D_A^2$ . The thick solid line shows the best-fit relation of  $P(\sigma_p|M_{SZ})$  with the intrinsic scatter shown as the green band. The other lines show several predictions of velocity bias. The dash-dotted line shows the prediction of Munari et al. (2013), the dotted line shows the prediction of Lau et al. (2010), the blue solid line shows the prediction of Saro et al. (2013), the long-dashed line shows the prediction from Old et al. (2013), and the blue short-dashed line shows the velocity bias for high-mass galaxies from Guo et al. (2015).

mass calibration yields reasonable agreement with the *Planck* CMB results, thus implying no need for massive neutrinos (Mantz et al. 2015). The good agreement between our measured velocity dispersions and those predicted by the *Planck* SZ masses (assuming little velocity bias) supports the mass calibration used in the *Planck* SZ analysis. Our results therefore support the possibility of massive neutrinos as a solution to the CMB-SZ tension.

Experimental measurements of neutrino oscillations place a lower limit of  $\Sigma m_\nu > 0.06\text{eV}$  [95% confidence level] (Capozzi et al. 2014). Constraints from the power spectrum of the Lyman- $\alpha$  forest from BOSS observations yield upper limits of  $\Sigma m_\nu < 0.98\text{ eV}$ , or  $< 0.16\text{ eV}$  when combined with *Planck* CMB data (Palanque-Delabrouille et al. 2015). Thus, massive neutrinos remain a plausible solution to the CMB-SZ tension, but the required masses may produce tension with constraints from the Lyman- $\alpha$  forest.

## 5. CONCLUSIONS

The *Planck* satellite has produced a dramatic increase in the number of galaxy clusters with SZ mass estimates. Because the catalog includes many nearby clusters and covers the entire sky, many clusters in the *Planck* catalog have existing mass estimates from galaxy dynamics. Here we measure 7,721 new redshifts in 24 clusters to obtain a large SZ-selected sample of 123 clusters with both dynamical and SZ mass estimates. To date, this

is the largest sample of clusters used to compare velocity dispersions and SZ mass estimates. We focus on a SZ-complete sample of 83 clusters.

The measured velocity dispersions agree well with the predicted velocity dispersions from the cluster masses in the *Planck* SZ catalog and the virial scaling relation of dark matter particles. The cosmological parameters based on *Planck* CMB observations are not consistent with the mass function based on masses from the *Planck* SZ catalog. One way to resolve this tension is to allow for mass bias in the SZ masses; large mass bias ( $M_{SZ} \approx 0.58 M_{true}$ ) is required to reconcile the CMB and SZ results. Such large mass bias is strongly disfavored by our results.

In principle, velocity bias could allow galaxy velocity dispersions to agree with the virial scaling relation for dark matter particles based on strongly biased SZ masses. However, no recent estimates of the amount of velocity bias are consistent with the large velocity bias ( $b_v \approx 0.77$ ) required for this scenario. In fact, some models of velocity bias have  $b_v > 1$ , a possibility that would further aggravate the tension between a possible SZ mass bias and our measured velocity dispersions.

Departures from a standard  $\Lambda$ CDM cosmological model could resolve the tension between CMB and SZ cosmological parameter estimates. For example, significant neutrino masses would decrease the amplitude of the power spectrum on cluster scales relative to the normalization from the CMB (Planck Collaboration et al. 2014a). In this scenario, *Planck* cluster masses could have little bias, and the excellent agreement between the measured velocity dispersions and the virial scaling relation of dark matter particles would require that galaxy velocity bias is small (i.e.,  $b_v \approx 1$ ).

Future work on the equilibrium dynamics of cluster galaxies can test the possibility of large velocity bias: if large velocity bias is present, a Jeans analysis should reveal that the cluster masses are larger than inferred by virial scaling relations (or by the caustic technique). Future simulations of the evolution of galaxies within clusters could test whether large velocity bias is plausible. If not, our results suggest that the tension between cosmological parameters derived from CMB and SZ data may require extensions to the standard  $\Lambda$ CDM cosmological model. Observations of SZ-selected clusters at higher redshift could measure the evolution of cluster scaling relations and provide further insight into the origin of the CMB-SZ tension.

We thank Jim Bartlett and Nabila Aghanim for advice on using the *Planck* SZ catalogs. MJG is supported by the Smithsonian Institution. AD acknowledges support from the grant Progetti di Ateneo/CSP TO Call2 2012 0011 “Marco Polo” of the University of Torino, the INFN grant InDark, the grant PRIN 2012 “Fisica Astroparticellare Teorica” of the Italian Ministry of University and Research. We thank Susan Tokarz for reducing the spectroscopic data and Perry Berlind and Mike Calkins for assisting with the observations. We also thank the telescope operators at the MMT and Nelson Caldwell for scheduling Hectospec queue observations.

*Facilities:* MMT (Hectospec), FLWO:1.5m (FAST)

## APPENDIX

## BAYESIAN PARAMETER ESTIMATION

Define the likelihood  $p(D|\theta, M)$  the probability of measuring the set of data  $D$  when the model  $M$  is described by the set of parameters  $\theta$ ; the prior  $p(\theta|M)$  is the probability that the set  $\theta$  occurs. We are interested in estimating the probability density function (PDF) of the parameters  $\theta$  given our data set  $D$

$$p(\theta|D, M) = \frac{p(D|\theta, M)p(\theta|M)}{p(D|M)}. \quad (\text{A1})$$

Given the model  $M$ , we need to assume the likelihood  $p(D|\theta, M)$  and the prior  $p(\theta|M)$ , whereas  $p(D|M)$  is a trivial normalization factor.

In this work, we are interested in describing our data with linear correlations between pairs  $(X, Y)$  of the logarithm of the observables. In general, a number of unknown hidden variables produces a scatter in the linear correlation  $Y = a + bX$ . We model this scatter with a single parameter, the intrinsic dispersion  $\sigma_{\text{int}}$ . Therefore, given a measure  $X_i$  with uncertainty  $\sigma_{X_i}$ , the probability of measuring  $Y_i$  with uncertainty  $\sigma_{Y_i}$  is  $p(Y_i, \sigma_{Y_i}|\theta, X_i, \sigma_{X_i})$ , where  $\theta = \{a, b, \sigma_{\text{int}}\}$ . We assume the Gaussian likelihood

$$p(D|\theta, M) = \prod_i \frac{1}{(2\pi\sigma_i^2)^{1/2}} \exp\left[-\frac{(Y_i - a - bX_i)^2}{2\sigma_i^2}\right] \quad (\text{A2})$$

where

$$\sigma_i^2 = \sigma_{\text{int}}^2 + \sigma_{Y_i}^2 + b^2\sigma_{X_i}^2. \quad (\text{A3})$$

We assume independent flat priors for both  $a$  and  $b$ . For the intrinsic dispersion  $\sigma_{\text{int}}$ , which is positive defined, we assume

$$p(\sigma_{\text{int}}|M) = \frac{\mu^r}{\Gamma(r)} x^{r-1} \exp(-\mu x) \quad (\text{A4})$$

where  $x = 1/\sigma_{\text{int}}^2$ , and  $\Gamma(r)$  is the usual gamma function. This PDF describes a variate with mean  $r/\mu$ , and variance  $r/\mu^2$ . We set  $r = \mu = 10^{-5}$  which guarantees an almost flat prior.

To estimate the parameter PDF  $p(\theta|D, M)$ , we perform a Markov Chain Monte Carlo (MCMC) sampling with the code APEMoST developed by Johannes Buchner and Michael Gruberbauer (Buchner & Gruberbauer 2011; Gruberbauer et al. 2009). We obtain a fairly complete sampling with  $2 \times 10^6$  MCMC iterations. The boundaries of the parameter space were set to  $[-100, 100]$  for  $a$  and  $b$ , and  $[0.01, 100]$  for  $\sigma_{\text{int}}$ . The initial seed of the random number generator was set with the `bash` command `GSL_RANDOM_SEED=$RANDOM`.

As the three best-fit parameters  $a$ ,  $b$ , and  $\sigma_{\text{int}}$  of the Bayesian analysis, we adopt the medians derived from the posterior PDF  $p(\theta|D, M)$ . Likewise, we adopt the boundaries of the 68% confidence levels around the medians as the uncertainties on these best-fit parameters.

## REFERENCES

- Adelman-McCarthy, J. K., et al. 2008, *ApJS*, 175, 297  
Ahn, C. P., et al. 2014, *ApJS*, 211, 17  
Andersson, K., et al. 2011, *ApJ*, 738, 48  
Andreon, S. 2010, *MNRAS*, 407, 263  
Applegate, D. E., et al. 2014, *MNRAS*, 439, 48  
Benson, B. A., et al. 2013, *ApJ*, 763, 147  
Biviano, A., & Girardi, M. 2003, *ApJ*, 585, 205  
Biviano, A., Murante, G., Borgani, S., Diaferio, A., Dolag, K., & Girardi, M. 2006, *A&A*, 456, 23  
Bocquet, S., et al. 2015, *ApJ*, 799, 214  
Böhringer, H., Burwitz, V., Zhang, Y.-Y., Schuecker, P., & Nowak, N. 2005, *ApJ*, 633, 148  
Böhringer, H., et al. 2000, *ApJS*, 129, 435  
—. 2004, *A&A*, 425, 367  
Bonamente, M., Joy, M., LaRoque, S. J., Carlstrom, J. E., Nagai, D., & Marrone, D. P. 2008, *ApJ*, 675, 106  
Bonamente, M., Landry, D., Maughan, B., Giles, P., Joy, M., & Nevalainen, J. 2013, *MNRAS*, 428, 2812  
Buchner, J., & Gruberbauer, M. 2011, APEMoST (Automated Parameter Estimation and Model Selection Toolkit), <http://apemost.sourceforge.net/>, commit from 2011-02-10  
Bullock, J. S., et al. 2001, *MNRAS*, 321, 559  
Capozzi, F., Fogli, G. L., Lisi, E., Marrone, A., Montanino, D., & Palazzo, A. 2014, *Phys. Rev. D*, 89, 093018  
Cypriano, E. S., Lima Neto, G. B., Sodré, Jr., L., Kneib, J.-P., & Campusano, L. E. 2005, *ApJ*, 630, 38  
Czapon, N. G., et al. 2015, *ApJ*, 806, 18  
Danese, L., de Zotti, G., & di Tullio, G. 1980, *A&A*, 82, 322  
Diaferio, A. 1999, *MNRAS*, 309, 610  
—. 2009, ArXiv e-prints, arXiv/0901.0868  
Diaferio, A., Geller, M. J., & Rines, K. J. 2005, *ApJ*, 628, L97  
Ebeling, H., Edge, A. C., Bohringer, H., Allen, S. W., Crawford, C. S., Fabian, A. C., Voges, W., & Huchra, J. P. 1998, *MNRAS*, 301, 881  
Evrard, A. E., et al. 2008, *ApJ*, 672, 122  
Fabricant, D., Cheimets, P., Caldwell, N., & Geary, J. 1998, *PASP*, 110, 79  
Fabricant, D., et al. 2005, *PASP*, 117, 1411  
Faltenbacher, A., & Diemand, J. 2006, *MNRAS*, 369, 1698  
Geller, M. J., Diaferio, A., Rines, K. J., & Serra, A. L. 2013, *ApJ*, 764, 58  
Gifford, D., & Miller, C. J. 2013, *ApJ*, 768, L32  
Gruberbauer, M., Kallinger, T., Weiss, W. W., & Guenther, D. B. 2009, *A&A*, 506, 1043  
Guo, H., et al. 2015, *MNRAS*, 446, 578  
Hasselfield, M., et al. 2013, *J. Cosmology Astropart. Phys.*, 7, 8  
Henry, J. P., Evrard, A. E., Hoekstra, H., Babul, A., & Mahdavi, A. 2009, *ApJ*, 691, 1307  
Hikage, C., & Yamamoto, K. 2015, ArXiv e-prints  
Hoekstra, H., Hartlap, J., Hilbert, S., & van Uitert, E. 2011, *MNRAS*, 412, 2095  
Hoekstra, H., Herbonnet, R., Muzzin, A., Babul, A., Mahdavi, A., Viola, M., & Cacciato, M. 2015, *MNRAS*, 449, 685  
Hoekstra, H., et al. 2001, *ApJ*, 548, L5  
Hwang, H. S., Geller, M. J., Diaferio, A., Rines, K. J., & Zahid, H. J. 2014, *ApJ*, 797, 106  
Israel, H., Schellenberger, G., Nevalainen, J., Massey, R., & Reiprich, T. H. 2015, *MNRAS*, 448, 814  
Kurtz, M. J., & Mink, D. J. 1998, *PASP*, 110, 934  
Lau, E. T., Nagai, D., & Kravtsov, A. V. 2010, *ApJ*, 708, 1419  
MacCrann, N., Zuntz, J., Bridle, S., Jain, B., & Becker, M. R. 2015, *MNRAS*, 451, 2877

- Mahdavi, A., Hoekstra, H., Babul, A., Bildfell, C., Jeltama, T., & Henry, J. P. 2013, *ApJ*, 767, 116
- Mamon, G. A., Biviano, A., & Boué, G. 2013, *MNRAS*, 429, 3079
- Mantz, A., Allen, S. W., Ebeling, H., Rapetti, D., & Drlica-Wagner, A. 2010a, *MNRAS*, 406, 1773
- Mantz, A., Allen, S. W., Rapetti, D., & Ebeling, H. 2010b, *MNRAS*, 406, 1759
- Mantz, A. B., et al. 2015, *MNRAS*, 446, 2205
- Marrone, D. P., et al. 2009, *ApJ*, 701, L114
- Melin, J.-B., & Bartlett, J. G. 2014, *ArXiv e-prints*
- Motl, P. M., Hallman, E. J., Burns, J. O., & Norman, M. L. 2005, *ApJ*, 623, L63
- Munari, E., Biviano, A., Borgani, S., Murante, G., & Fabjan, D. 2013, *MNRAS*, 430, 2638
- Nagai, D., Vikhlinin, A., & Kravtsov, A. V. 2007, *ApJ*, 655, 98
- Navarro, J. F., Frenk, C. S., & White, S. D. M. 1997, *ApJ*, 490, 493
- Nelson, K., Lau, E. T., & Nagai, D. 2014, *ApJ*, 792, 25
- Old, L., Gray, M. E., & Pearce, F. R. 2013, *MNRAS*, 434, 2606
- Old, L., et al. 2014, *MNRAS*, 441, 1513
- Palanque-Delabrouille, N., et al. 2015, *J. Cosmology Astropart. Phys.*, 2, 45
- Perrott, Y. C., et al. 2014, *ArXiv e-prints*
- Piffaretti, R., Arnaud, M., Pratt, G. W., Pointecouteau, E., & Melin, J.-B. 2011, *A&A*, 534, A109
- Planck Collaboration et al. 2011, *A&A*, 536, A11
- . 2013a, *A&A*, 550, A130
- . 2013b, *A&A*, 550, A131
- . 2014a, *A&A*, 571, A20
- . 2014b, *A&A*, 571, A29
- . 2015a, *ArXiv e-prints*
- . 2015b, *ArXiv e-prints*
- Rines, K., & Diaferio, A. 2006, *AJ*, 132, 1275
- Rines, K., Diaferio, A., & Natarajan, P. 2007, *ApJ*, 657, 183
- . 2008, *ApJ*, 679, L1
- Rines, K., Geller, M. J., & Diaferio, A. 2010, *ApJ*, 715, L180
- Rines, K., Geller, M. J., Diaferio, A., & Kurtz, M. J. 2013, *ApJ*, 767, 15
- Rines, K., Geller, M. J., Kurtz, M. J., & Diaferio, A. 2003, *AJ*, 126, 2152
- Rozo, E., et al. 2010, *ApJ*, 708, 645
- Ruel, J., et al. 2014, *ApJ*, 792, 45
- Saro, A., Mohr, J. J., Bazin, G., & Dolag, K. 2013, *ApJ*, 772, 47
- Schellenberger, G., Reiprich, T. H., Lovisari, L., Nevalainen, J., & David, L. 2015, *A&A*, 575, A30
- Serra, A. L., & Diaferio, A. 2013, *ApJ*, 768, 116
- Serra, A. L., Diaferio, A., Murante, G., & Borgani, S. 2011, *MNRAS*, 412, 800
- Sifón, C., et al. 2013, *ApJ*, 772, 25
- Sunyaev, R. A., & Zeldovich, Y. B. 1972, *Comments on Astrophysics and Space Physics*, 4, 173
- Vikhlinin, A., et al. 2009a, *ApJ*, 692, 1033
- . 2009b, *ApJ*, 692, 1060
- von der Linden, A., et al. 2014, *MNRAS*, 443, 1973
- Wu, H.-Y., Hahn, O., Evrard, A. E., Wechsler, R. H., & Dolag, K. 2013, *MNRAS*, 436, 460
- Wyman, M., Rudd, D. H., Vanderveld, R. A., & Hu, W. 2014, *Physical Review Letters*, 112, 051302
- Zwicky, F. 1933, *Helv. Phys. Acta*, 6, 110
- . 1937, *ApJ*, 86, 217